Improved Scaling Relationships for Seismic Moment and Average Slip of Strike-Slip Earthquakes Incorporating Fault-Slip Rate, Fault Width, and Stress Drop

John G. Anderson*[1], Glenn P. Biasi[2], Stephen Angster[3], and Steven G. Wesnousky[1]

ABSTRACT

We develop a self-consistent scaling model relating magnitude M_w to surface rupture length (L_E), surface displacement D_E, and rupture width W_E, for strike-slip faults. Knowledge of the long-term fault-slip rate S_F improves magnitude estimates. Data are collected for 55 ground-rupturing strike-slip earthquakes that have geological estimates of L_E, D_E, and S_F, and geophysical estimates of W_E. We begin with the model of Anderson *et al.* (2017), which uses a closed form equation for the seismic moment of a surface-rupturing strike-slip fault of arbitrary aspect ratio and given stress drop, $\Delta\tau_C$. Using W_E estimates does not improve M_w estimates. However, measurements of D_E plus the relationship between $\Delta\tau_C$ and surface slip provide an alternate approach to study W_E. A grid of plausible stress drop and width pairs were used to predict displacement and earthquake magnitude. A likelihood function was computed from within the uncertainty ranges of the corresponding observed M_w and D_E values. After maximizing likelihoods over earthquakes in length bins, we found the most likely values of W_E for constant stress drop; these depend on the rupture length. The best-fitting model has the surprising form $W_E \propto \log L_E$—a gentle increase in width with rupture length. Residuals from this model are convincingly correlated to the fault-slip rate and also show a weak correlation with the crustal thickness. The resulting model thus supports a constant stress drop for ruptures of all lengths, consistent with teleseismic observation. The approach can be extended to test other observable factors that might improve the predictability of magnitude from a mapped fault for seismic hazard analyses.

KEY POINTS

- We estimate earthquake magnitude from fault length and slip rate, and the assumption of constant stress drop.
- For internally consistent length, width, slip, and constant stress drop, width increases as log length.
- Internally consistent relationships support improved rupture forecasts and synthetic seismogram generation.

Supplemental Material

INTRODUCTION

Fault scaling relations to estimate magnitude (M_w) based on geological and geophysical observations are an essential component for seismic hazard analysis. The seismic hazard analysis combines the magnitude and fault geometry with the distance to the site to estimate the ground motion at the site, often using a ground-motion prediction equation but sometimes using some other type of ground-motion model such as synthetic seismograms. A complete seismicity model for a study site includes the magnitude and rates of all earthquakes that are relevant to the hazard at the site. Geological observations can provide the fault location, length of the observed surface trace and a sense of motion, the slip rate on the fault, and also sometimes an estimate of the local surface slip in one or more recent earthquakes. Geophysical data may give some insight on the depth of brittle faulting. These data can be used to estimate

1. Nevada Seismological Laboratory, University of Nevada, Reno, Nevada, https://orcid.org/0000-0002-8882-6039 (JGA); https://orcid.org/0000-0002-6734-6183 (SGW); 2. U.S. Geological Survey, Pasadena, California, U.S.A., https://orcid.org/0000-0003-0940-5488 (GPB); 3. U.S. Geological Survey, Seatle, Washington, U.S.A., https://orcid.org/0000-0001-9250-8415 (SA)

*Corresponding author: jga@unr.edu

Cite this article as Anderson, J. G., G. P. Biasi, S. Angster, and S. G. Wesnousky (2021). Improved Scaling Relationships for Seismic Moment and Average Slip of Strike-Slip Earthquakes Incorporating Fault-Slip Rate, Fault Width, and Stress Drop, *Bull. Seismol. Soc. Am.* **XX**, 1–14, doi: 10.1785/0120210113

rupture lengths and locations of possible earthquakes on the fault. Examples of studies that use scaling relationships that translate length and other parameters into estimates of the magnitudes of possible earthquakes include Stirling *et al.* (2002), Field *et al.* (2014), Petersen *et al.* (2014), and Haller *et al.* (2015).

The history of scaling relations for magnitude from fault parameters goes back to Tocher (1958) and Iida (1959). Kanamori and Anderson (1975), provided a theoretical basis for why the magnitude should be proportional to the log of the rupture length or rupture area. The ideas in that paper, preceding the definition of the moment magnitude scale (Kanamori, 1977), extend easily to the moment magnitude (e.g., Leonard, 2010). Readers are referred to studies by Leonard (2010) and Hanks and Bakun (2014) for details.

Anderson *et al.* (1996), superseded by Anderson *et al.* (2017; hereafter, ABW17), develop models relating rupture length to magnitude and extended the model to consider the effect of fault-slip rate on fault scaling. Stirling and Anderson (2018) carried out a test of the ABW17 model for data from New Zealand. Observations supporting a slip-rate effect on magnitude scaling can be traced to Kanamori and Allen (1986) and Scholz *et al.* (1986). Anderson *et al.* (1996) first quantified this effect as a function of slip rate using the data that were available to them at that time. ABW17, using a significantly expanded data set and removing some equivocal data points, confirmed that for strike-slip faults the geological slip rate of the fault can significantly reduce uncertainty in the estimate of M_w compared to length alone. The logarithmic dependence on slip rate that they proposed is consistent with the logarithmic increase in static friction with time since the last rupture observed by Dieterich (1972). Initial length–magnitude relations in ABW17 followed earlier work by assuming a quasi-circular rupture growth mode for moderate earthquakes that transitions to a second mode in which ruptures grow in length alone, because the seismogenic thickness is fixed and presumably fully participating. The second growth mode leads to increasing model stress drop with length—a prediction inconsistent with teleseismic observations and studies over large ranges of magnitudes (e.g., Allmann and Shearer, 2009; Baltay *et al.*, 2010, 2011). Where magnitude dependence of estimated stress drop is observed, studies suggest that it may be due to imperfections in the sensitive adjustments for attenuation (e.g., Anderson, 1986; Abercrombie, 1995; Ide *et al.*, 2003). Thus the two-mode models of ABW17 significantly improved magnitude predictions from rupture length. However, these models are not entirely satisfactory, because of the inconsistent definition of stress drop between the two growth modes and because of the inconsistencies of their implied stress drop with instrumental observations.

The idea of seeking a scaling relation with constant stress drop is not new (e.g., Shaw, 2009). The fault rupture model by Chinnery (1963, 1964) is an alternative length–magnitude relationship with internally consistent definitions and a constant stress drop. Instead of an ad hoc transition between rupture growth modes, the model provides a closed form relationship among L_E, W_E, D_E, and $\Delta\tau_C$ for surface rupturing earthquakes of any dimension. The model M3 of ABW17 incorporates the fault rupture model of Chinnery. After adding a slip-rate adjustment, model M3 in ABW17 predicts observed values of M_w as well as the other models and resolved the stress-drop contradiction posed by teleseismic observations.

This article evaluates whether the M3 constant stress-drop model to estimate M_w from fault length and slip rate can be improved to provide estimates of average slip by incorporating an improved model for the fault width and stress drop. The addition of a model for which the width is consistent with average slip D_E and M_w increases the usefulness of this model for generating synthetic seismograms and for estimates of fault displacement hazard. We consider only earthquakes that have predominantly a strike-slip focal mechanism. As seen by ABW17, the available data for earthquakes with predominantly reverse or normal mechanisms are not sufficiently numerous or well distributed to support a similar analysis.

BACKGROUND

Seismic moment and moment magnitude

Seismic moment (M_0) is defined as

$$M_0 = \mu L_E W_E D_E, \tag{1}$$

in which L_E is the rupture length in the earthquake, W_E is the rupture width of the earthquake, D_E is the average slip on the fault during the earthquake, and μ is the shear modulus. Moment magnitude can be viewed as a transformation of variables from the seismic moment. The transformation equation is implicit in Kanamori (1977) and recommended by the International Association for Seismology and Physics of the Earth's Interior (International Association of Seismology and Physics of the Earth's Interior [IASPEI], 2005, 2013; Bormann *et al.*, 2012) for seismic network practice:

$$M_w = \frac{2}{3}\log\left[\frac{M_0}{M_0(0)}\right]. \tag{2}$$

Here, $M_0(0)$ is the seismic moment of an earthquake with moment magnitude of zero, $10^{16.1}$ dyn · cm, or $10^{9.1}$ N · m. This article uses units consistent with $\log M_0(0) = 16.1$ to be consistent with seismic moments sourced from the Global Centroid Moment Tensor (Global CMT) project.

ABW17 M3

ABW17 discussed three scaling relations to estimate M_w from L_E and geological fault slip rate S_F. The third of these M3 was the first magnitude scaling relation to be based on the analytical surface rupture model of Chinnery (1963, 1964). The Chinnery formulation allows a single parametric form

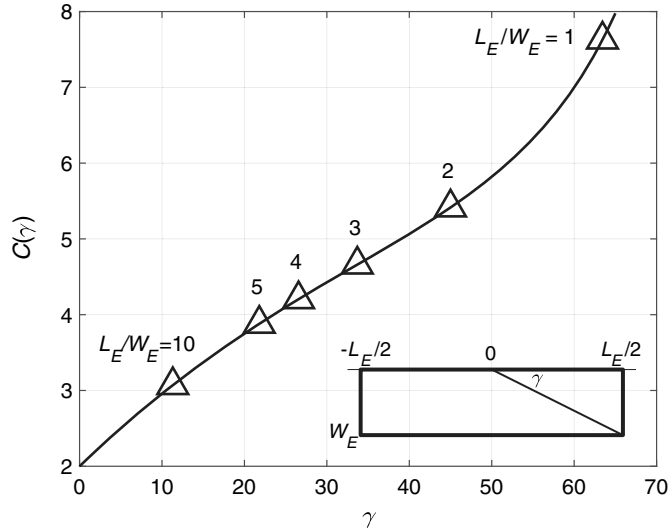

Figure 1. Rupture model geometry (inset) and geometric factor $C(\gamma)$ (equation 4) used in this article. Triangles show selected aspect ratios L_E/W_E.

to represent ruptures of all aspect ratios, from equant to extremely long, with a single stress drop (Fig. 1). Moment magnitude expressed in this formulation is

$$M_0 = \frac{2\pi}{C(\gamma)} \Delta\tau_C L_E W_E^2, \tag{3}$$

in which

$$C(\gamma) = 2\cos\gamma + 3\tan\gamma - \frac{\cos\gamma\sin\gamma(3 + 4\sin\gamma)}{(1 + \sin\gamma)^2}, \tag{4}$$

and

$$\tan\gamma = \frac{2W_E}{L_E}. \tag{5}$$

The stress-drop parameter $\Delta\tau_C$ identified by Chinnery (1963, 1964) gives the stress drop at the top center of a rectangular fault that ruptures the surface and has uniform slip over its entire surface. The magnitude scaling in M3 is written explicitly by substituting equation (3) into equation (2) and adusting the magnitude for slip rate with the term $c_2 \log\frac{S_F}{S_0}$, in which S_0 is a reference slip rate and c_2 controls the slope:

$$M_w = \frac{2}{3}\log\Delta\tau_C + \frac{2}{3}\log\left[\frac{L_E W_E^2}{C(\gamma)}\right] - \frac{2}{3}\log\frac{M_0(0)}{2\pi} + c_2\log(S_F/S_0). \tag{6}$$

Table 1 summarizes the parameters suggested by ABW17 for model M3.

Substituting the definition of M_0 from equation (1) into equation (3) we obtain

$$\Delta\tau_C = \frac{C(\gamma)}{2\pi}\mu\frac{D_E}{W_E}, \tag{7}$$

TABLE 1
Parameters for Models M3 and M4 for Strike-Slip Earthquakes

Property	Model M3	Model M4
W_E (km)	15 for (L_E > 57 km), L_E/3.8 for ($L_E \le$ 57 km)	$11.8 + 9.18\log(\frac{L_E}{100})$
$\Delta\tau_C$	24.9 ± 1.1 bars, 2.49 ± 0.11 MPa	28 bars, 2.8 MPa
c_2	−0.170 ± 0.029	−0.20 ± 0.01
S_0	4.8 mm/yr	6.3 mm/yr
σ_L	0.236	0.227
σ_S	0.214	0.185

Common features of both the models:

$$M_0 = \frac{2\pi}{C(\gamma)}\Delta\tau_C L_E W_E^2,$$

$$C(\gamma) = 2\cos\gamma + 3\tan\gamma - \frac{\cos\gamma\sin\gamma(3 + 4\sin\gamma)}{(1 + \sin\gamma)^2},$$

$$\tan\gamma = \frac{2W_E}{L_E},$$

$$M_w = \frac{2}{3}\log\left[\frac{M_0}{M_0(0)}\right] + c_2\log\left[\frac{S_F}{S_0}\right].$$

σ_L: Standard deviation of $\delta_{L,i}$, the difference between the observed magnitude and the model estimated magnitude using $S_F = S_0$.
σ_S: Standard deviation of $\delta_{S,i}$, the difference between the observed magnitude and the model estimated magnitude using the observed values of S_F for each fault.

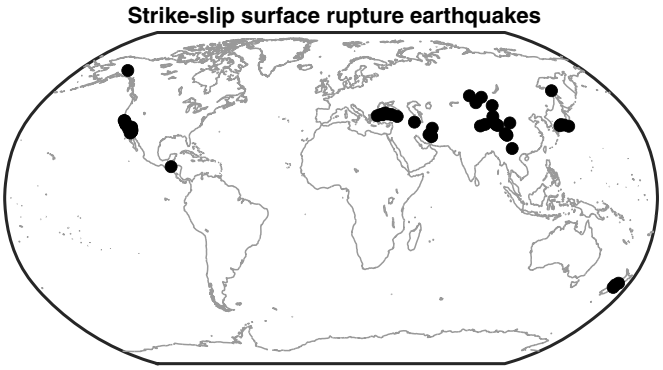

Figure 2. Locations of the strike-slip earthquakes used in this study.

as the stress drop for a surface rupturing earthquake for the Chinnery model. For a long fault $\gamma \to 0$ and $C(\gamma) \to 2$, so for a long strike-slip fault, $\Delta\tau_C \approx \frac{1}{\pi}\mu\frac{D_E}{W_E}$. Stress drop in the better-known model of Kanamori and Anderson (1975) for a long strike-slip fault is given by $\Delta\tau_{KA} \approx \frac{2}{\pi}\mu\frac{D_E}{W_E}$, which is a factor of two larger. For small earthquakes, one might expect $W_E \propto L_E$, in which case $C(\gamma)$ is constant. The geometric factor $C(\gamma)$ modulates a transition in the slope of the scaling from $\sim 2\log L_E$ for the range of magnitudes in which L_E is similar to W_E to earthquakes with high aspect ratio ruptures scaling as $\sim\frac{2}{3}\log L_E$ in which rupture increases in length with no change in width.

Benchmarks for the quality of data fit in this study are the standard deviations of the magnitude residuals in model M3, as given in Table 1.

DATA

We use geological observations of rupture length, average slip, and fault slip rate as estimates of L_E, D_E, and S_F, respectively. Seismic moment is obtained from seismic observations when available. Our data set includes 55 large ($M_w > 5.79$) global strike-slip earthquakes occurring between 1848 and 2010. The data are summarized in Tables 2 and 3. The supplemental material gives details. Figure 2 shows epicenters of the considered earthquakes. The selected events occur in western United States, Guatamala, countries in the Middle East, China, Mongolia, Russia, Japan, and New Zealand. Further details about data selection are reviewed in the following sections.

TABLE 2
Earthquakes from 1966 to 2010 Used in This Study

Number	References*	Earthquake Name	Date (yyyy/mm/dd)	M_w	L_E (km)	D_E (m)	S_F (mm/yr)	W_E (km)
1	3	Darfield	2010/09/04	7.12	30	2.55	0.25	13.5
2	4	Yushu	2010/04/14	6.84	52	1.0	12	11
3	5	El Mayor–Cucapah	2010/04/04	7.26	117	2.15	2.5	15.5
4	8	Chuya	2003/09/27	7.25	70	2	0.5	15
5	9	Denali	2002/11/03	7.85	340	3.6	12.4	15
6	10	Kunlun	2001/11/14	7.73	450	3.3	10	15
7	11	Duzce	1999/11/12	7.09	40	2.1	15	15.1
8	12	Hector Mine	1999/10/16	7.13	48	4	0.6	11
9	14	Izmit	1999/08/17	7.49	145	1.1	12	15
10	15	Fandoqa	1998/03/14	6.57	22	1.1	2	17
11	16	Manyi	1997/11/08	7.50	170	2.3	3	20
12	17	Sakhalen Island (Neftegorsk)	1995/05/27	7.02	40	3.9	4	17
13	19	Landers	1992/06/28	7.19	77	2.3	0.4	16.5
14	22	Rudbar	1990/06/20	7.36	80	2.48	1	15
15	24	Superstition Hills	1987/11/24	6.62	25	0.54	3	11
16	28	Morgan Hill	1984/04/24	6.15	20	1	5.2	11
17	31	Sirch	1981/07/28	7.15	65	0.13	4.3	17
18	34	Daofu	1981/01/24	6.74	44	0.4	12	14
19	36	Imperial Valley	1979/10/15	6.40	36	0.41	17	12
20	37	Coyote Lake	1979/08/06	5.79	14	0.17	11.9	9
21	40	Bob-Tangol	1977/12/19	5.81	19.5	0.15	4	14
22	41	Montagua	1976/02/04	7.54	230	1.08	12	15
23	42	Luhuo	1973/02/06	7.45	90	2.5	14	15
24	44	Tonghai	1970/01/04	7.23	50	1.7	2	12
25	45	Dasht-e-Bayaz	1968/08/31	7.11	80	1.79	5	13.5
26	46	Borrego Mtn.	1968/04/09	6.63	33	0.13	6.7	10
27	47	Mudurnu Valley	1967/07/22	7.29	80	0.9	18	16
28	48	Parkfield	1966/06/28	6.18	28	0.43	30	13

M_w, L_E, D_E, S_F, W_F: These are the preferred values from the supplemental table. See the supplemental table for uncertainty ranges and references.
*Event number in the supplemental table and Figure 2, mainly following the numbering in ABW17.

TABLE 3
Earthquakes from 1800 to 1963 Used in This Study

Number	References	Earthquake Name	Date (yyyy/mm/dd)	M_w	L_E (km)	D_E (m)	S_F (mm/yr)	W_E (km)
29	49	Alake Lake	1963/04/19	6.97	40	1.9	12	16
30	52	Gobi Altai	1957/12/04	8.10	260	4.0	1.0	17
31	53	San Miguel	1956/02/14	6.60	20	0.4	0.3	15
32	56	Gonen–Yenice	1953/03/18	7.27	60	2.9	6.8	13
33	58	Gerede–Bolu	1944/02/01	7.35	155	2.1	18	13
34	59	Tosya	1943/11/26	7.57	275	2.5	19	13
35	60	Tottori	1943/09/10	6.92	33	0.6	0.3	16
36	61	Niksar–Erbaa	1942/12/20	6.84	50	1.66	19	13
37	62	Imperial Valley	1949/05/19	7.10	60	3.87	17	8.5
38	63	Erzincan	1939/12/25	7.81	330	4.2	19	13
39	64	Tosuo Lake–Huashixia	1937/01/07	7.65	150	4.1	11	15
40	65	Parkfield	1934/06/08	6.17	25	0.8	30	14
41	66	Long Beach	1933/03/10	6.40	22	1.0	1.1	17.5
42	67	Changma	1932/12/25	7.56	149	2.3	5.0	16
43	68	Fuyun	1931/08/10	7.89	160	6.3	0.3	20
44	69	North Izu	1930/11/25	6.89	28	1.1	2.4	12
45	71	Tango	1927/03/07	7.04	35	1.0	0.3	14
46	72	Luoho-Qiajiao (Daofu)	1923/03/24	7.32	80	2.5	10	24
47	73	Haiyuan	1920/12/16	7.99	237	10	4.5	17
48	76	San Francisco	1906/04/18	7.92	497	1.5	21	14
49	77	Bulnay	1905/07/23	8.35	375	8.9	3	18
50	78	Laguna Salada	1892/02/23	7.20	42	5.3	2.5	12
51	80	Nobi/Mino–Owari	1891/10/28	7.44	80	3.1	1.6	15
52	87	Canterbury	1888/09/01	7.12	65	2	14	12
53	83	Hayward	1868/10/21	6.92	61	1.9	8	15
54	84	Fort Tejon	1857/01/09	7.83	339	4.7	25	15
55	85	Marlborough	1848/10/16	7.52	134	5.3	5.6	13.5

Criteria for data selection

Ideally, earthquakes are considered for this study if reliable, independent measurements are available for the rupture length, average slip, seismic moment, and fault-slip rate. We initially also sought reliable estimates of the depth of faulting, but in the end the depth of faulting was relegated to a confirmatory position.

Methods to determine seismic moment

For this project, seismic moments are preferred where determined by geophysical means, that is, from interpretation of seismograms or from geodetic deformation. Since 1977, the Global CMT project has used a relatively consistent methodology to estimate the seismic moments for every earthquake considered in this study. However, other studies sometimes have the advantage of using local data and models. The range of estimates using alternative data or methods contribute estimates of the uncertainty.

For older earthquakes, such as the 1857 Fort Tejon, California, earthquake, M_0 and thus M_w are by necessity estimated from L_E and D_E for an assumed value of W_E. It may seem circular to use these events to find an optimized model for M_w, W_E, and $\Delta\tau_C$. However, M_w is not sensitive to a fairly large change in estimates of W_E. A doubling of W_E increases M_w by only 0.2 magnitude units, and the full range of W_E is smaller than that. This uncertainty in M_w is incorporated in the analysis. Because secondary faulting contributes to seismological estimates of moment, this may introduce a bias to underestimate the magnitudes of these early events compared to recent events. Importantly, the events in this category have well-constrained slip rates that are important to constrain the slip rate dependence in the model.

Methods to determine fault length

Two alternative definitions of rupture length were considered. The first is to define L_E as the length of the primary surface ruptured zone, measured from end to end. For large earthquakes, rupture can be curved on a small circle as for the 2002 Denali, Alaska, earthquake (number 5 in Table 2). The alternative is to include the lengths of secondary ruptures and branch splays in the total rupture length. The difference can be large. A recent example is the 2010 Darfield, New Zealand, earthquake (number 1 in Table 2) in which the surface rupture was about 30 km long (Barrell *et al.*, 2011; Elliott *et al*, 2012), but aftershocks and Interferometric Synthetic Aperture Radar (InSAR) observations revealed significant slip on additional faults oriented at high angles to this rupture totaling about 16 km in total length (Elliott *et al.*, 2012), as well as subsurface

slip extending the length of the main rupture. An older example is the 1905 Bulnay, Mongolia, earthquake (number 49 in Table 3), in which the main rupture was about 388 km in length, but rupture occurred also on secondary faults of 80 and 35 km length (Choi *et al.*, 2018).

This study adopts the first definition, taking the rupture length as the end-to-end length of the affected area. This is adopted with consideration of the potential uses of this model, in which the length of the main trace of a fault is what the geologist can measure. It is the controlling scale for displacement to develop. It is difficult for a user to guess which secondary faults, if any, might rupture in an earthquake. In the example of the Darfield earthquake, it is complicated and/or nearly impossible to recognize and measure all the secondary faults from geological observations. Similarly, Choi *et al.* (2018) mention for the 1905 Bulnay, Mongolia, rupture that they recognized additional shorter branches but did not quantify them. Given the complexity of faulting, it can be ambiguous to determine whether a feature should be included or not. Finally, adding the secondary features may not make very much difference in the end. Again, using the Bulnay event as an example, the moment of the major secondary branches is in the range $[6-8]\cdot 10^{27}$ dyn · cm, whereas the moment of the main contribution is at least $[30-67]\cdot 10^{27}$ dyn · cm (Schlupp and Cisternas, 2007). Adding the secondary rupture to the larger estimate of the contribution from the main fault changes the moment magnitude by only 0.07. In ABW17, the standard deviation of magnitude estimates is over 0.2 magnitude units (Table 1). In a site-specific study of fault hazard, proximity to a secondary rupture may be important, but for this study their omission has at the most very modest impacts on results.

The rupture length can be measured by geological mapping or by geophysical techniques, which might be based on either InSAR or the extent of early aftershocks. Wells and Coppersmith (1994) have compared and contrasted these two measurements. They conclude that geological measurement of surface rupture length is, on average, about 0.75 of the subsurface length measured by the length of the aftershock zone, although the ratio increases toward one for longer ruptures. Where available, we prefer and use geological measurements of rupture length. For older earthquakes such measurements are more available and more reliable than aftershock locations. In addition, the intended application of the model is to estimate magnitudes from observed surface ruptures of past earthquakes or from mapped fault lengths, so using geological observations here is more consistent.

Methods to determine slip rate

Slip rates were obtained primarily from geologic slip-rate studies on the fault experiencing rupture. Where estimates cover different geologic time periods, emphasis is given to the Holocene rates. The supplemental data table and reference list give citations for individual estimates.

Methods to determine fault width

Unlike the fault length, the fault width can only be determined through the use of geophysical techniques. Unfortunately, depth of aftershocks provides reliable estimates of rupture width only for recent earthquakes (Wells and Coppersmith, 1994). For some earthquakes, the maximum depth of microearthquakes in the vicinity of the mainshock or proximal geodetic information is available, but the majority lack any such modern geophysical evidence. In addition, even the modern smaller events in this study may have the most slip in a patch that is much smaller than the depth of aftershocks. In this case, we consider the depth of aftershocks an upper bound on W_E. Width estimates from geophysical measurements are thus used here only to compare with the developed width model.

Methods to determine average slip

In general, geological materials along the surface rupture are highly variable and highly nonlinear, so surface slip gives an imperfect representation of the deeper slip on the fault. Tables 2 and 3 use the average slip based on geological observations. With this approach, the preferred values of D_E may be smaller than the slip at depth, especially for the shorter ruptures. Uncertainties, which are tabulated in the supplemental material, have been fully considered in the modeling.

PROPERTIES OF THE DATA

The rupture lengths and fault-slip rates of the selected events (Fig. 2), as summarized in Tables 2 and 3, are plotted in Figure 3. Both rupture length L_E and slip rate S_F of these events are relatively uniformly distributed, between 20 and 500 km for rupture length and 0.3 and 30 mm/yr for slip rate, and do not seem to show a dependence on one another. This low correlation is suited to our present objective of a relationship for estimating magnitude, like ABW17, from $\log L_E$ and $\log S_F$.

MAXIMUM-LIKELIHOOD APPROACH AND RESULTS

We develop a method to use the better resolved parameters M_w, L_E, and D_E to investigate less well-resolved parameters $\Delta\tau_C$ and W_E. The structure of equations (1)–(6) suggests using a maximum-likelihood approach. A grid of plausible values of τ_C and W_E can be considered. For each pair of values, incorporating uncertainties in L_E, the probability distributions of M_0 and D_E for each earthquake can be found. Then, considering uncertainties in the data, the likelihood of this pair of $\Delta\tau_C$ and W_E can be found for each earthquake. Higher likelihoods correspond to choices of $\Delta\tau_C$ and W_E that are most consistent with resolved parameters for a given earthquake. Log likelihoods summed over all earthquakes provide a global picture of the viability of different combinations of $\Delta\tau_C$ and W_E.

To correctly calculate the likelihoods, we first describe how uncertainties in M_w and D_E are represented. We illustrate how

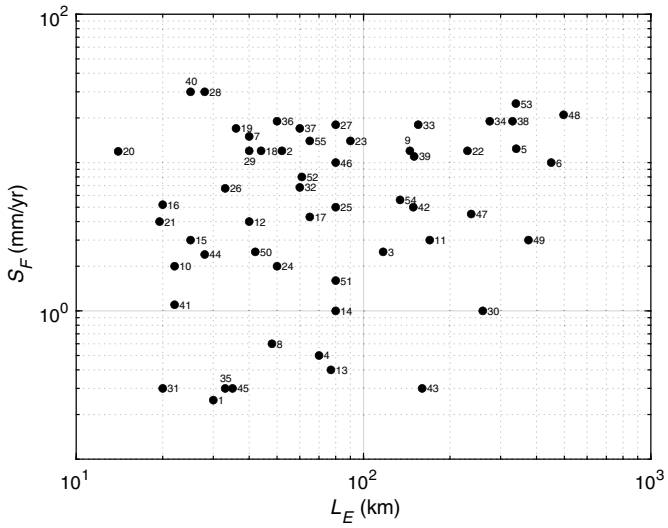

Figure 3. Slip rate and rupture length of strike-slip earthquakes considered in this study.

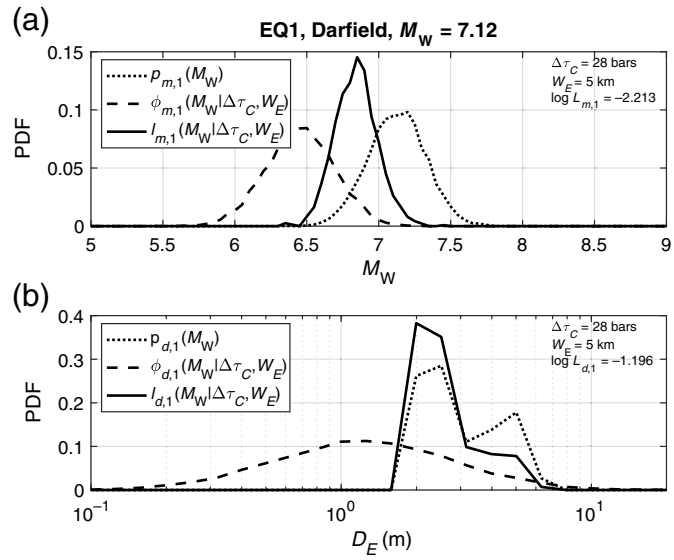

Figure 4. Comparison of likelihood magnitude and displacement density distributions to observed values for the Darfield earthquake assuming trial stress drop $\Delta\tau_C = 28$ bars (2.8 MPa), trial width $W_E = 5$ km, and length uncertainty σ_{3L}. (a) Magnitude-likelihood density distribution $l_{m,1}$ underpredicts the observed magnitude estimate (dotted line). (b) Likelihood $l_{d,1}$ for the assumed stress drop, and width overpredicts the observed displacement.

we represent uncertainty in moment magnitude and total slip using the 2010 Darfield, New Zealand, earthquake (Table 2, event 1). Considering fault slip D_E first, the best estimate is 2.55 m, and the uncertainty range is 1.9–5.8 m (Table S1, available in the supplemental material to this article). A probability distribution for D_E, $p_{d,i}(D_E)$, illustrated in the lower frame of Figure 4, is constructed by assuming that the best estimate is median of the distribution. The index i indicates that the function is defined for the ith earthquake. The 50% probability of larger slip is distributed uniformly between the median and the maximum value. Similarly, the 50% probability of smaller slip is distributed uniformly between the median and the minimum value. The uncertainties in the observed M_w, in the upper frame of Figure 4, are applied in the same way around a preferred magnitude M_w 7.1. In developing $p_{m,i}(M_w)$, an additional uncertainty is applied modeled by a normal distribution function with uncertainty of 0.2 magnitude units on top of the range given in Table S1. Because the distributions of $p_{m,i}(M_w)$ and $p_{d,i}(D_E)$ do not follow an analytical form, their plots are drawn from the envelope of 10,000 Monte Carlo trials following the rules just described. The distribution of these data constants $p_{m,i}(M_w)$ and $p_{d,i}(D_E)$ are plotted on a logarithmic scale (dotted lines, Fig. 4).

For earthquake i, the probability distribution of the model estimate of the magnitude $\varphi_{m,i}(M_w|\Delta\tau_C, W_E)$ and the slip $\phi_{d,i}(D_E|\Delta\tau_C, W_E)$ starts with equation (3). In addition to $\Delta\tau_C$ and W_E, equation (3) needs a rupture length to find the model seismic moment. The observed length is treated as uncertain and described by a probability distribution. This distribution is defined with 50% probability of values distributed uniformly between the best estimate and the minimum estimate, and 50% probabiltiy of values distributed uniformly between the best estimate and the maximum estimate. For a pair of values of $\Delta\tau_C$ and W_E, in 10,000 Monte Carlo trials, a length drawn from the length distribution and the consequent seismic moment is calculated using equation (3), followed by a slip calculated using equation (1). The distributions of magnitude and slip are determined by these Monte Carlo trials. The model distributions $\phi_{m,i}$ and $\phi_{d,i}$ for the Darfield earthquake are shown as dashed lines in Figure 4.

The likelihood density function for magnitude measures the probability of a value of M_w having come from the assumed values for τ_C and W_E:

$$l_{m,i}(M_w|\Delta\tau_C, W_E) = p_{m,i}(M_w)\phi_{m,i}(M_w|\Delta\tau_C, W_E). \quad (8)$$

The corresponding likelihood density function of rupture displacement D_E is given by:

$$l_{d,i}(D_E|\Delta\tau_C, W_E) = p_{d,i}(D_E)\phi_{d,i}(D_E|\Delta\tau_C, W_E). \quad (9)$$

In Figure 4, these density functions have been normalized to unit area to enhance visibility, but in reality their areas are much smaller. Their areas $L_{m,i}(\Delta\tau_C, W_E)$ and $L_{d,i}(\Delta\tau_C, W_E)$ are the likelihoods that the selected values of $\Delta\tau_C$ and W_E fit the magnitude and slip of earthquake i, including uncertainties. The equations are

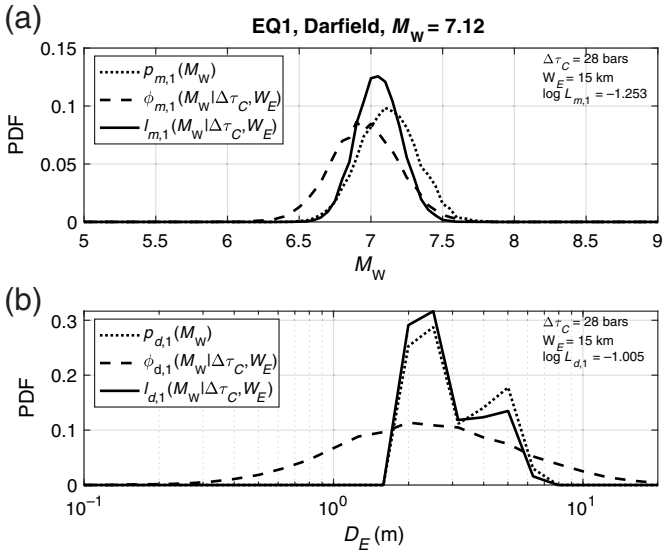

Figure 5. Compared to Figure 4, trial stress drop $\Delta\tau_C = 28$ bars (2.8 MPa) and trial width $W_E = 15$ km produce better fits of the likelihood of (a) displacement and (b) magnitude for the Darfield earthquake case.

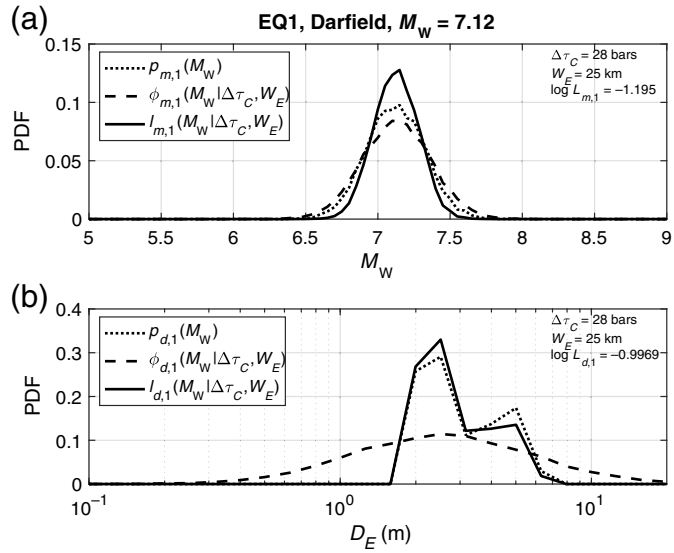

Figure 6. Further increase of the width estimate to $W_E = 25$ km with $\Delta\tau_C = 28$ bars (2.8 MPa) only slightly improves likelihood density fits to observed (a) magnitude and (b) displacement.

$$L_{m,i}(\Delta\tau_C, W_E) = \int l_{m,i}(M_w|\Delta\tau_C, W_E)dM_w, \qquad (10)$$

and

$$L_{d,i}(\Delta\tau_C, W_E) = \int l_{d,i}(D_E|\Delta\tau_C, W_E)dD_E. \qquad (11)$$

The logarithms of these likelihoods are given in the respective frames of Figure 4. Giving magnitude and slip estimates equal weight, the total likelihood of earthquake i being modeled by equation (3) with selected values of $\Delta\tau_C$ and W_E is given by

$$\log[L_i(\Delta\tau_C, W_E)] = \log[L_{m,i}(\Delta\tau_C, W_E)] + \log[L_{d,i}(\Delta\tau_C, W_E)]. \qquad (12)$$

Figures 4–6 illustrate the variation in likelihoods for three values of W_E and a constant $\Delta\tau_C = 28$ bars (2.8 MPa). For a trial value $W_E = 5$ km (Fig. 4), the model predicted and observed magnitudes are not aligned, so the likelihood of that this choice of W_E led to the observed magnitude is less than 10^{-2}. In contrast, when W_E is increased to 15 km (Fig. 5), the predicted and observed magnitudes are substantially aligned, and the likelihood is increased. Increasing W_E from from 15 to 25 km (Fig. 6) has less effect on the predicted magnitude, because the magnitude increases as the log of the width. As a result, the likelihood of the 25 km model is only slightly increased. When the same range of trial values of W_E is appled to predict D_E, the prediction is quite wide, so the likelihood fitting D_E is somewhat less selective, but still shows a preference for the 15 or 25 km widths.

We explore for systematic relations among earthquake parameters by evaluating the likelihoods of events of similar rupture length. We divide earthquakes into eight groups of increasing length. Figure 7 shows the number of earthquakes in each group. For group g, a combined likelihood for a given value of $\Delta\tau_C$ and W_E is calculated as

$$\log L_g(\Delta\tau_C, W_E) = \sum_{i\in g} \log L_i(\Delta\tau_C, W_E). \qquad (13)$$

The likelihoods in equation (13) can be contoured, and, in principle, the combination of $\Delta\tau_C$ and W_E with the highest value is the best model for this group.

The contours for earthquakes in two sample distance groups are shown in Figures 8 and 9. Two features are evident. The first is that stress drop and rupture width are strongly correlated, such that a larger width and low-stress drop can have nearly the same likelihood as a small width and larger stress drop. The trade-off is not linear but rather suggests a hyperbolic trade-off. The second point is that the trade-off is quite different for the two selected ranges of rupture length.

Given the seismological observation that stress drop is relatively independent of magnitude, profiles for constant $\Delta\tau_C$ across Figures 8 and 9, and the other rupture length ranges were constructed. The profiles corresponding to Figures 8 and 9 at $\Delta\tau_C = 28$ bars (2.8 MPa) are shown in Figures 10 and 11, respectively. Likelihoods were extrapolated between calculated points near their peaks using a cubic spline (MATLAB function "interp1" with the "cubic" interpolation method), and the maximum of the group likelihood was used as the value of W_E for the group. Uncertainties were estimated

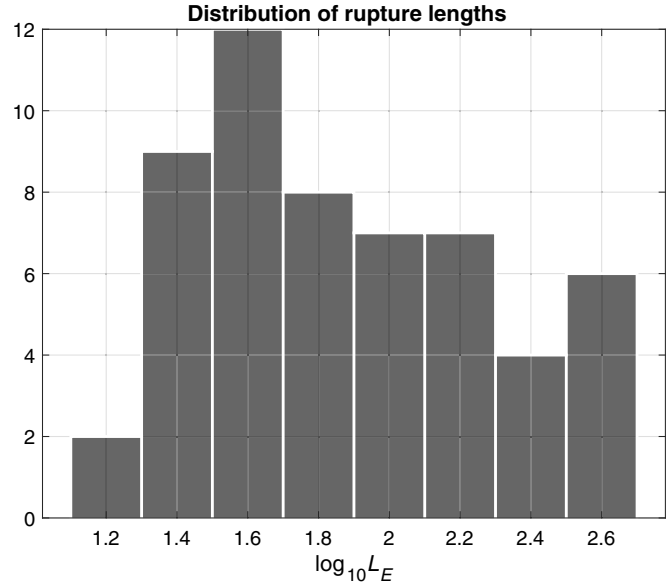

Figure 7. Number of ruptures in length bins used for likelihood analysis.

by, rather arbitrarily, finding the range of W_E at 75% of the peak value.

When the peaks and uncertainties from the profiles' likelihood in Figures 10 and 11 are plotted on a semilog axis versus length group in Figure 12, a clear trend of increasing "best" W_E is observed. The maximum-likelihood value of W_E as a function of L_E is fit in Figure 12 by

$$W_E = 11.9 + 8.69 \log\left(\frac{L_E}{100}\right), \tag{14}$$

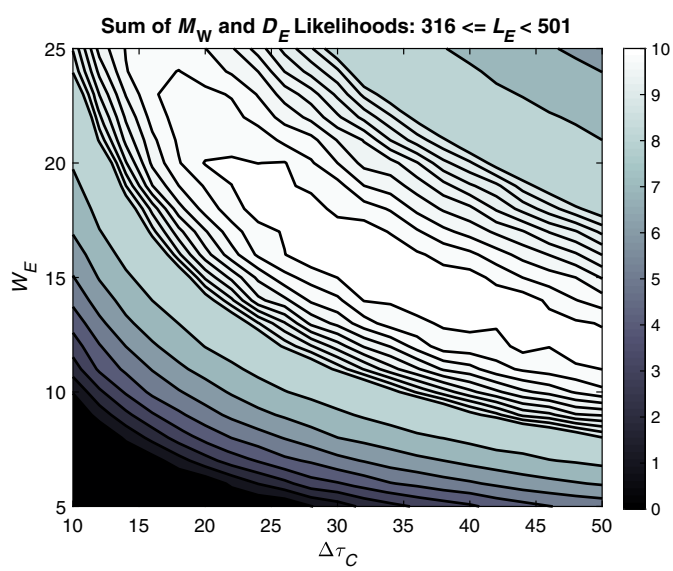

Figure 9. Equivalent of Figure 8, for events with rupture length between 315 and 500 km. The color version of this figure is available only in the electronic edition.

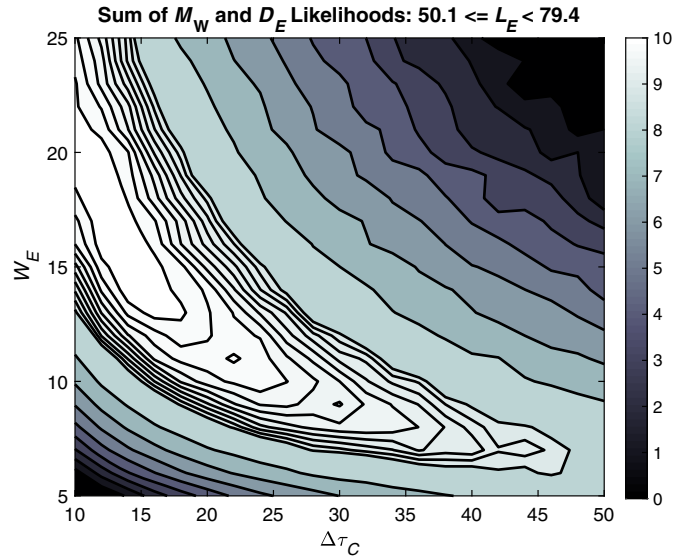

Figure 8. Contours of model likelihoods for events with rupture lengths from 50 to 79 km. Without loss of generality, for clarity of the presentation, a constant value is added to all values of $\log L$ to cause the maximum value on the plot to equal 10.0. Contours separated by shaded regions are separated by differences of 1.0 in $\log L$. For $\log L > 9$, the contours are separated by differences of 0.1 in $\log L$. Values of $\log L < 0$ are shaded the same as $\log L = 0$. The color version of this figure is available only in the electronic edition.

with units of L_E and W_E in kilometers. The standard deviation of the misfit of equation (12) is $\sigma_W = 0.529$ km. The minimum value of σ_W over the set of all trial values of $\Delta\tau_C$ appears to be between 28 bars (used in Fig. 12) and 30 bars (2.8–3.0 MPa). Not shown, linear and power-law equations,

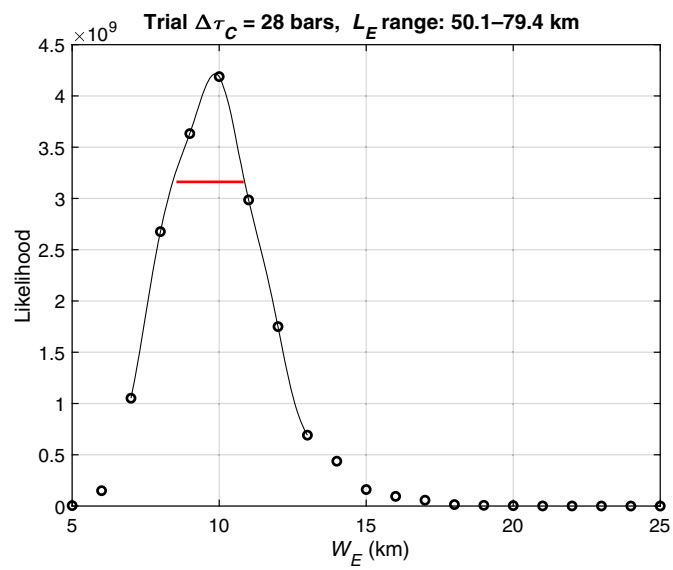

Figure 10. Likelihood of W_E conditioned on $\Delta\tau_C = 28$ bars for earthquakes with L_E between 50 and 79 km. The horizontal line indicates the range used as the uncertainty of W_E, estimated by the rupture width range at 75% of the maximum likelihood. The color version of this figure is available only in the electronic edition.

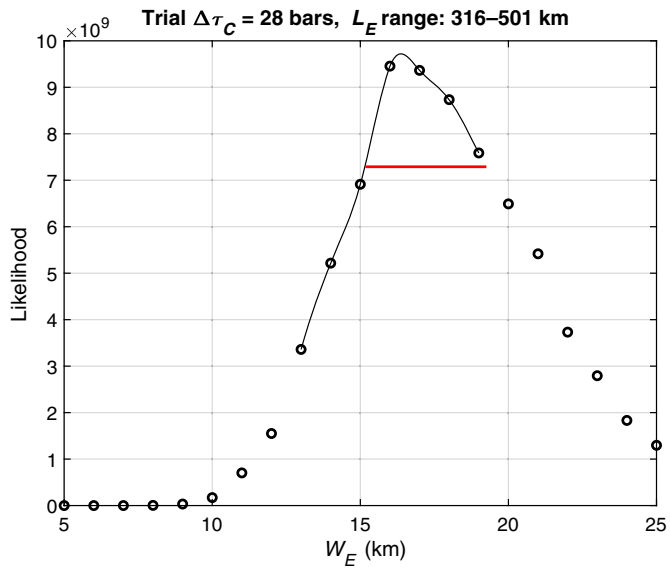

Figure 11. Likelihood of W_E conditioned on $\Delta\tau_C = 28$ bars for earthquakes with L_E between 315 and 500 km. The horizontal line indicates the range used as the uncertainty of W_E, estimated by the rupture width range at 75% of the maximum likelihood. The color version of this figure is available only in the electronic edition.

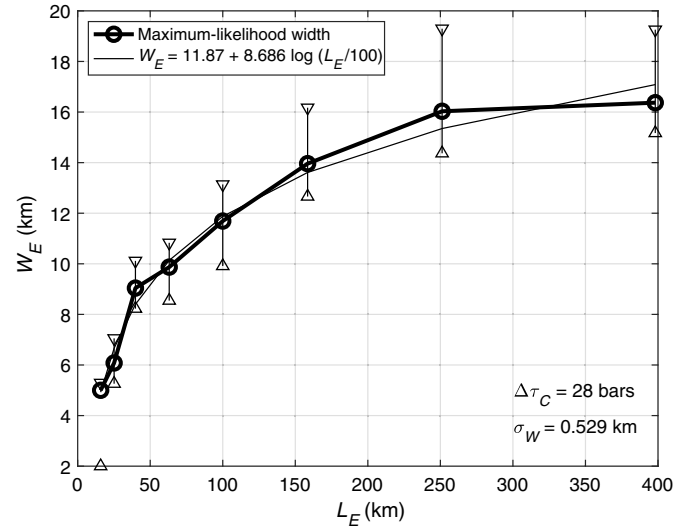

Figure 12. Estimated rupture widths as a function of rupture length for $\Delta\tau_C = 28$ bars. Triangles and connecting lines show the uncertainty in W_E as estimated in Figure 11.

$W_E = a + bL_E$ and $\log W_E = a + b\log(\frac{L_E}{100})$, respectively, were also tested. For all $\Delta\tau_C$, the standard deviation of the linear model is larger. The standard deviation of the power law is also considerably larger for all values of τ_C under 40 bars (4 MPa). When it is smaller, the fault width is smaller than the widths shown in Figure 12, and the slip is generally higher than the observations. To be specific, for a trial value of $\Delta\tau_C = 40$ bars (4 MPa), the width for the longest earthquakes is only 14 km, which seems unreasonable considering the estimates in Tables 2 and 3.

EVALUATION

The functional relation between W_E and L_E in equation (14) is compared to geologic observation in Figure 13. The widths for large rupture lengths (≥100 km) and $\Delta\tau_C = 28$ bars (2.8 MPa) are roughly consistent, on average, with reported W_E values. This provides some confirmation that a scaling model implementing a constant stress drop can yield reasonable widths and magnitudes, as predicted by teleseismic stress-drop observations. Increasing stress drop with rupture length (Hanks and Bakun, 2014) would not yield this consistency. Equation (14) underestimates reported widths for short ruptures. We next substitute equation (14) into the Chinnery model magnitude and stress-drop equations (equations 3–6) to compare (Fig. 14) the mean slip predictions with the preferred geologic surface slip from Tables 2 and 3. As for rupture width estimates, the predicted displacements are generally consistent with observations for large events, but the agreement is poor for short rupture lengths. Causes for the poor agreement of geologic displacement and width with predictions will be discussed subsequently.

Substituting equation (14) in the Chinnery magnitude relation (equation 3) yields what we call model 4 (M4). We use M4 to estimate magnitudes as a function of rupture length (Fig. 15). In this case, the agreement of model and data appears to be satisfactory. Magnitude residuals versus rupture length in Figure 15 show no trend in misfit (Fig. 16). In contrast, magnitude residuals as a function of slip rate (Figure 17) do show a trend toward lower magnitude with higher slip rate. The least-squares fit to the residuals in Figure 17 finds that

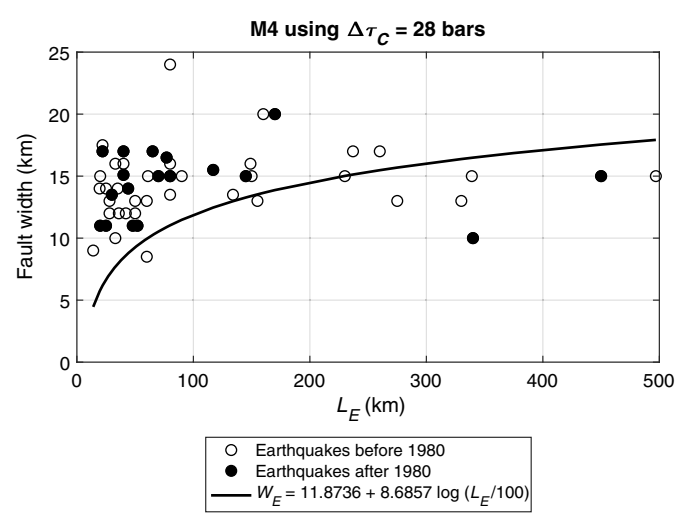

Figure 13. Preferred estimates of surface rupture length and fault width inferred from aftershock or small earthquake depths, compared with the model in equation (14).

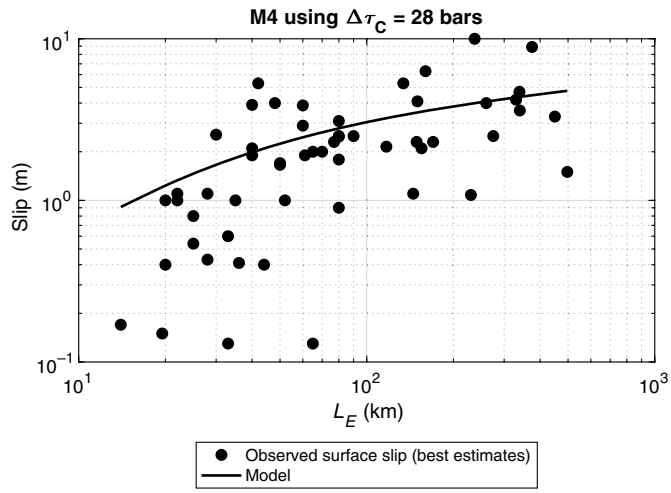

Figure 14. The best estimates of surface slip from rupture length, based on model M4, compared with observed values as given in Tables 2 and 3.

$$\delta M_w = -0.20 \log\left(\frac{S_F}{S_0}\right), \tag{15}$$

in which reference rate $S_0 = 6.3$ mm/yr. As in the previous analysis of ABW17, for strike-slip faults a higher slip rate is significantly correlated with a more negative magnitude residual. The best fit to the points in Figure 17 has the slope 0.215 ± 0.042. However, the mean slope of 10^5 calculations using randomized slip rates within their uncertainty range is 0.203 ± 0.011. These uncertainty values are found using only the best estimates of magnitude and rupture length. Because the two estimates of the slope are consistent within uncertainties, we round the slope to two significant figures in equation (15). The slope of the linear regression in Figure 17 is slightly greater than the slope found in ABW17 (Table 1) but the same as the preferred value found by Anderson *et al.* (1996). Table 1 also shows the residuals of this new model and the corresponding residuals from M3 of ABW17. The uncertainty in predicting the magnitude from length alone is slightly decreased in model M4 compared to M3 (σ_L, Table 1) and decreased more significantly (from $\sigma_S = 0.214$ for M3 to $\sigma_S = 0.185$ for M4; Table 1) when predicting the magnitude using both length and slip rate.

Magnitude residuals adjusted for the fault-slip rate show a slight correlation with crustal thickness based on the global model Crust 1.0 (Laske *et al.*, 2013; Fig. 18). The reason for this test is that we expect the crustal thickness to be inversely correlated with heat flow, and the thickness of the brittle layer to also be correlated to heat flow. There is a weak correlation and a small reduction in the standard deviation, but the slope is

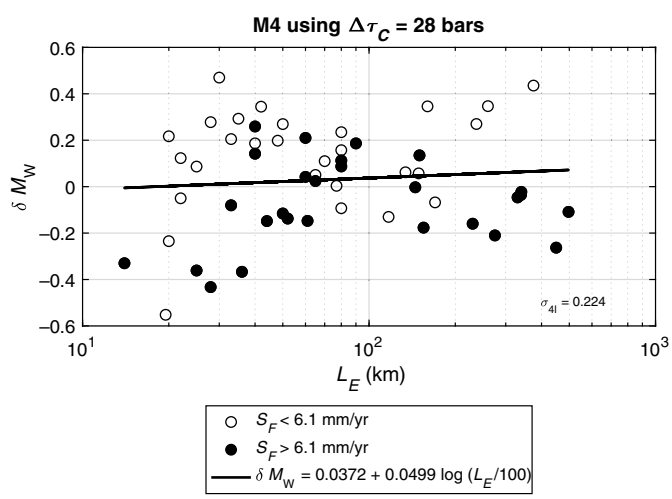

Figure 16. Magnitude residuals as a function of L_E.

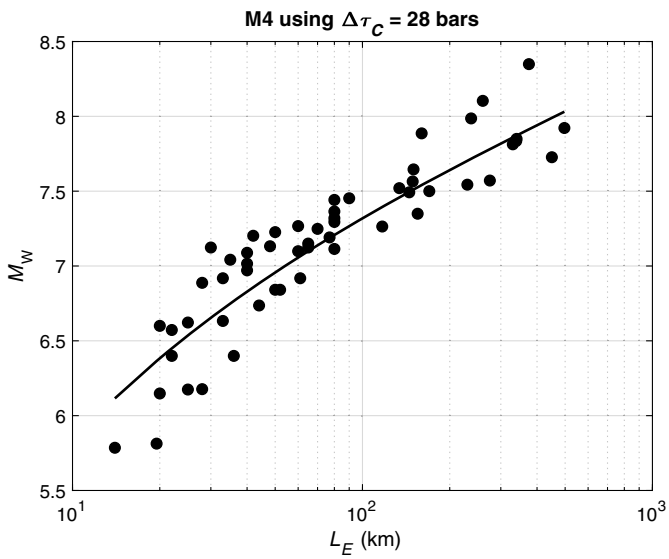

Figure 15. Magnitude from rupture length for $\Delta\tau_C = 28$ bars.

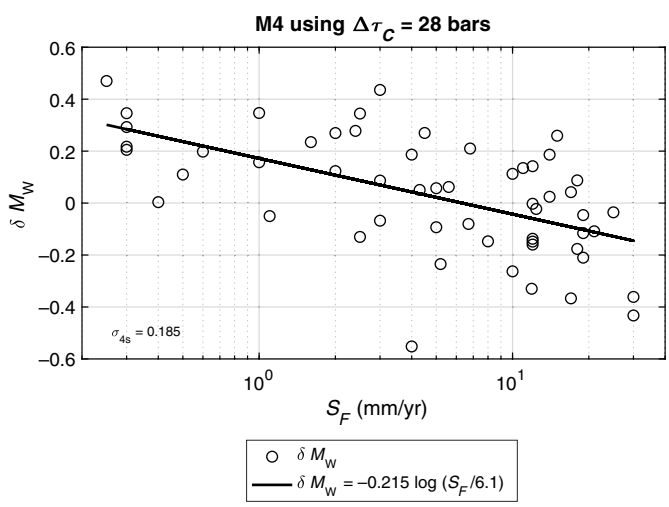

Figure 17. Magnitude residuals as a function of the geological slip rate of the fault S_F.

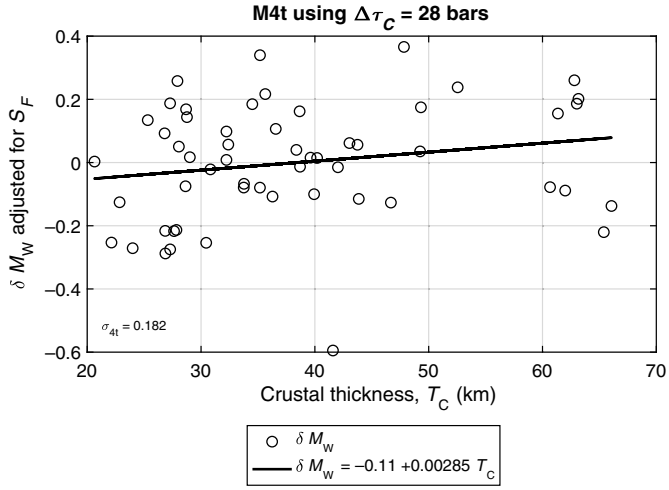

Figure 18. Magnitude residuals, adjusted for slip rate, correlated with the thickness of the continental crust.

not significantly different from zero (<95% confidence), and this reduction in sigma is not statistically significant.

DISCUSSION AND CONCLUSIONS

The primary advantage of model M4 with width proportional to the log of length compared with model M3 is that M4 provides a self-consistent model for the rupture length and slip. This is achieved by the approximation of stress drop $\Delta\tau_C$ as a constant to find an empirical relationship between L_E and W_E. However, because constant stress drop is reasonably well supported by the teleseismic observations (e.g., Allmann and Shearer, 2009), the assumption of a constant stress drop in model M4 can be viewed as a first-order measure to incorporate that observation. Seismologically, we recognize that earthquakes do not all have the same stress drop but use a single value of stress drop as an empirical mean to represent the actual distribution. In some confirmation of this assumption, we note that model M4 also fits our rupture parameter data better than model M3.

For seismic hazard analysis there are some advantages to a scaling model with internally consistent magnitude, rupture length, and slip. Consider a comprehensive seismic hazard analysis that develops of a set of earthquake rupture forecasts and then generates synthetic seismograms from each to build a set of ground-motion scenarios and corresponding seismic hazard curves (e.g., Graves *et al.*, 2011). An objective earthquake rupture forecast that allows for partial ruptures of the fault (e.g., Andrews and Schwerer, 2000; Field and Page, 2011; Field *et al.*, 2014) requires scaling relations to associate a magnitude and slip with each rupture. Then, the slip of each event is used to solve for occurrence rates, constrained by the observed fault-slip rate. It is helpful if the scaling used for this step is consistent with scaling of dynamic rupture properties used to generate the synthetic seismograms (e.g., Somerville *et al.*, 1999). For instance, Graves *et al.* (2011) had to make adjustments for scaling models that lacked this consistency. An internally consistent model such as model M4 might alleviate that need, although further investigation is needed to confirm that suggestion. Further investigation might also explore the extent to which uncertainties in stress drop improve modeling efforts through the correlations they imply for uncertainties in magnitude and slip.

An alternative approach to selecting model parameters, which would likely do about as well as our decision to use a constant $\Delta\tau_C$, is to select a constant value of W_E and then find optimum values of $\Delta\tau_C$ to model the data. This approach would find that the stress drop is an increasing function of the rupture length. Although fixing W_E would be mathematically feasible, the strength of the observations of roughly constant stress drop (e.g., Allmann and Shearer, 2009) persuaded us that it would not be worthwhile in practice.

Based on Figure 13, our model also does not fit the geophysically inferred values of W_E particularly well. However, we suggest that the small rupture widths at small magnitudes predicted by equation (14) are not unreasonable. Inversions for slip distributions of small events have found that the majority of slip on the faults takes place over a smaller depth range than the width of the seismogenic zone. For example, for the M_w 6.8 Yushu earthquake (L_E 50 km) Yang *et al.* (2015) found aftershocks to 13 km depth, but the largest slip patch found by waveform inversion extends from the surface only to 7 km depth and is thus quite consistent with equation (14). Similarly, overprediction by model M4 of rupture displacement for ruptures shorter than 50 km (Fig. 13) could be explained as an artifact of incomplete rupture to the surface. For both displacement and rupture width, we view model M4 as providing a new line of inquiry for understanding what actually slips during surface rupturing earthquakes and by how much.

The dependence of W_E on L_E (which is a new component to this M4 model) is not a complete surprise. In the limit of small magnitudes that are confined within the seismogenic crust, circular models are a standard approximation, so the "squaring" of the circle in the Chinnery rupture model leads to identical values. For the longest ruptures, some studies have recognized that W_E may increase with L_E (e.g., Rolandone *et al.*, 2004; Hillers and Wesnousky, 2008; Shaw and Wesnousky, 2008) and may penetrate below the seismogenic zone (King and Wesnousky, 2007; Jiang and Lapusta, 2016). Figures 1 and 2 of Leonard (2010) suggest a power-law relationship, but a power law is not as good a fit to our data as the log–linear relationship in equation (12). An interesting question is whether there is any theoretical basis for the relationship found in equation (14) and Figure 12. The fact that it is such a good fit is a surprise and suggests that there may be some physical basis for this result.

There are some obvious extensions to this model. The first is to extend the database with more recent earthquakes, and the

addition of older earthquakes as reliable fault-slip rates become developed. After that, this provides a framework to test other geophysical observables that should be expected to affect the width of the seismogenic zone. Heat flow is an obvious example. Our attempt to use crustal thickness as a proxy for heat flow did not show significant results, but direct heat flow observations may be more successful. For other ideas, one could also look for effects of lithology or total fault offset over geological time. In general, we anticipate that incorporating a strong theoretical basis and then seeking additional observables is the most promising way in the future to improve the predictability of magnitude from geological observations of fault length.

DATA AND RESOURCES

In addition to numerous detailed studies reported in the supplemental material, the following databases were consulted extensively in development of earthquake parameters in Tables 2 and 3. Seismic moments: Global CMT Project (https://www.globalcmt.org, last accessed December 2019). Earthquake locations: U. S. Geological Survey COMCAT (https://earthquake.usgs.gov/earthquakes/search/, last accessed December 2019), and International Seismological Center Bulletin (http://www.isc.ac.uk/iscbulletin/search/catalogue/, last accessed December 2019). Fault parameters: U.S. Geological Survey Fault and Fold Database: https://www.usgs.gov/natural-hazards/earthquake-hazards/faults?qt-science_support_page_related_con=4#qt-science_support_page_related_con (last accessed August 2021). The database has been revised and moved since it was last accessed for this study on December 2019. The IASPEI "Summary of magnitude working group recommendations on standard procedures for determining earthquake magnitudes from digital data" was accessed at: ftp://ftp.iaspei.org/pub/commissions/CSOI/Summary_WG_recommendations_20130327.pdf (last accessed December 2019). Crustal thickness reported by Laske *et al.* (2013): https://igppweb.ucsd.edu/~gabi/crust1.html#reference (last accessed February 2020).

DECLARATION OF COMPETING INTERESTS

The authors acknowledge that there are no conflicts of interest recorded.

ACKNOWLEDGMENTS

The authors thank Robert Graves and Annemarie Baltay for their very helpful reviews and thoughtful comments. This research was supported by the U.S. Geological Survey (USGS), Department of the Interior, under USGS Award Number G17AP00105.

REFERENCES

Abercrombie, R. (1995). Earthquake source scaling relationships from -1 to 5 M_L using seismograms recorded at 2.5-km depth, *J. Geophys. Res.* **100,** 24,015–24,036.

Allmann, B. P., and P. M. Shearer (2009). Global variations of stress drop for moderate to large earthquakes, *J. Geophys. Res.* **114,** no. B01310, doi: 10.1029/2008JB005821.

Anderson, J. G. (1986). Implication of attenuation for studies of the earthquake source, in *Earthquake Source Mechanics*, S. Das, J. Boatwright, and C. H. Scholz (Editors), Geophysical Monograph (Maurice Ewing Series 6), Vol. 37, American Geophysical Union, Washington, D.C., 311–318.

Anderson, J. G., G. P. Biasi, and S. G. Wesnousky (2017). Fault-scaling relationships depend on the average fault-slip rate, *Bull. Seismol. Soc. Am.* **107,** no. 6, 2561–2577.

Anderson, J. G., S. G. Wesnousky, and M. Stirling (1996). Earthquake size as a function of fault slip rate, *Bull. Seismol. Soc. Am.* **86,** 683–690.

Andrews, D. J., and E. Schwerer (2000). Probability of rupture of multiple fault segments, *Bull. Seismol. Soc. Am.* **90,** 1498–1506.

Baltay, A., S. Ide, G. Prieto, and G. Beroza (2011). Variability in earthquake stress drop and apparent stress, *Geopyhys. Res. Lett.* **38,** L06303, doi: 10.1029/2011GL046698.

Baltay, A., G. Prieto, and G. C. Beroza (2010). Radiated seismic energy from coda measurements and no scaling in apparent stress with seismic moment, *J. Geophys. Res.* **115,** no. B08314, doi: 10.1029/2009JB006736.

Barrell, D. J. A., N. J. Litchfield, D. B. Townsend, M. Quigley, R. J. Van Dissen, R. Cosgrove, S. C. Cox, K. Furlong, P. Villamor, J. G. Begg, *et al.* (2011). Strike-slip ground-surface rupture (Greendale Fault) associated with the 4 September 2010 Darfield earthquake, Canterbury, New Zealand, *Q. J. Eng. Geol. Hydrogeol.* **44,** 283–291, doi: 10.1144/1470-9236/11-034.

Bormann, P., S. Wendt, and D. DiGiacomo (2012). Chapter 3: Seismic sources and source parameters, in *New Manual of Seismological Observatory Practice (NMSOP-2)*, P. Bormann (Editor), IASPEI, GFZ German Research Centre for Geosciences, Potsdam, Germany, doi: 10.2312/GFZ.NMSOP-2_CH3, 10.2312/GFZ.NMSOP-2.

Chinnery, M. A. (1963). The stress changes that accompany strike-slip faulting, *Bull. Seismol. Soc. Am.* **53,** no. 5, 921–932.

Chinnery, M. A. (1964). The strength of the Earth's crust under horizontal shear stress, *J. Geophys. Res.* **59,** 2085–2089.

Choi, J.-H., Y. Klinger, M. Ferry, J.-F. Ritz, R. Kurtz, M. Rizza, L. Bollinger, B. Davaasambuu, N. Tsend-Ayush, and S. Demberel (2018). Geologic inheritance and earthquake rupture processes: The 1905 M 8 Tsetserleg-Bulnay strike-slip earthquake sequence, Mongolia, *J. Geophys. Res.* **123,** no. 2, 1925–1953, doi: 10.1002/2017JB013962.

Dieterich, J. H. (1972). Time dependent friction in rocks, *J. Geophys. Res.* **20,** 3690–3704.

Elliott, J. R., E. K. Nissen, P. C. England, J. A. Jackson, S. Lamb, Z. Li, M. Oehlers, and B. Parsons (2012). Slip in the 2010–2011 Canterbury earthquakes, New Zealand, *J. Geophys. Res.* **117,** no. B03401, doi: 10.1029/2011JB008868.

Field, E. H., and M. T. Page (2011). Estimating earthquake-rupture rates on a fault or fault system, *Bull. Seismol. Soc. Am.* **101,** 79–92, doi: 10.1785/ 0120100004.

Field, E. H., R. J. Arrowsmith, G. P. Biasi, P. Bird, T. E. Dawson, K. R. Felzer, D. D. Jackson, K. M. Johnson, T. H. Jordan, C. Madden, *et al.* (2014). Uniform California earthquake rupture forecast, version 3 (UCERF3)—The time-independent model, *Bull. Seismol. Soc. Am.* **104,** 1122–1180, doi: 10.1785/0120130164.

Graves, R., T. H. Jordan, S. Callaghan, E. Deelman, E. Field, G. Juve, C. Kesselman, P. Maechling, G. Mehta, K. Milner, *et al.* (2011). CyberShake: A physics-based seismic hazard model for Southern

California, *Pure Appl. Geophys.* **168,** 367–381, doi: 10.1007/s00024-010-0161-6.

Haller, K. M., M. P. Moschetti, C. S. Mueller, S. Rezaeian, M. D. Petersen, and Y. Zeng (2015). Seismic hazard in the Intermountain West, *Earthq. Spectra* **31,** no. S1, S149–S176.

Hanks, T. C., and W. H. Bakun (2014). M-log A models and other curiosities, *Bull. Seismol. Soc. Am.* **104,** 2604–2610, doi: 10.1785/0120130163.

Hillers, G., and S. G. Wesnousky (2008). Scaling relations of strike-slip earthquakes with different slip-rate-dependent properties at depth, *Bull. Seismol. Soc. Am.* **98,** 1085–1101, doi: 10.1785/0120070200.

International Association of Seismology and Physics of the Earth's Interior (IASPEI) (2005). Summary of magnitude working group recommendations on standard procedures for determining earthquake magnitudes from digital data, available at ftp://ftp.iaspei.org/pub/commissions/CSOI/summary_of_WG_recommendations_2005.pdf (last accessed August 2021).

International Association of Seismology and Physics of the Earth's Interior (IASPEI) (2013). Summary of magnitude working group recommendations on standard procedures for determining earthquake magnitudes from digital data, available at ftp://ftp.iaspei.org/pub/commissions/CSOI/Summary_WG_recommendations_20130327.pdf (last accessed August 2021).

Ide, S., G. C. Beroza, S. G. Prejean, and W. L. Ellsworth (2003). Apparent break in earthquake scaling due to path and site effects on deep borehole recordings, *J. Geophys. Res.* **108,** 2271, doi: 10.1029/2001JB001617.

Iida, K. (1959). Earthquake energy and earthquake fault, Nagoya University, *J. Earth Sci.* **7,** 98–107.

Jiang, J., and N. Lapusta (2016). Deeper penetration of large earthquakes on seismically quiescent faults, *Science* **352,** 1293–1297.

Kanamori, H. (1977). The energy release in great earthquakes, *J. Geophys. Res.* **82,** 2981–2987.

Kanamori, H., and C. R. Allen (1986). Earthquake repeat time and average stress drop, in *Earthquake Source Mechanics*, S. Das, J. Boatwright, and C. H. Scholz (Editors), Geophysical Monograph, Vol. 37, American Geophysical Union, Washington, D.C., 227–235.

Kanamori, H., and D. L. Anderson (1975). Theoretical basis of some empirical relations in seismology, *Bull. Seismol. Soc. Am.* **65,** no. 5, 1073–1095.

King, G. C. P., and S. G. Wesnousky (2007). Scaling of fault parameters for continental strike-slip earthquakes, *Bull. Seismol. Soc. Am.* **97,** 1833–1840.

Laske, G., G. Masters, Z. Ma, and M. E. Pasyanos (2013). Update on CRUST1.0: A 1-degree global model of Earth's crust, *Poster EGU2013-2658*, available at https://igppweb.ucsd.edu/gabi/crust1/laske-egu13-crust1.pdf (last accessed February 2020).

Leonard, M. (2010). Earthquake fault scaling: Relating rupture length, width, average displacement, and moment release, *Bull. Seismol. Soc. Am.* **100,** no. 5, 1971–1988, doi: 10.1785/0120090189.

Petersen, M. D., M. P. Moschetti, P. M. Powers, C. S. Mueller, K. M. Haller, A. D. Frankel, Y. Zeng, S. Rezaeian, S. C. Harmsen, O. S. Boyd, *et al.* (2014). Documentation for the 2014 Update of the United States national seismic hazard maps, *U.S. Geol. Surv. Open-File Rept. 2014-1091*, 243 pp.

Rolandone, F., R. Burgmann, and R. M. Nadeau (2004). The evolution of the seismic-aseismic transition during the earthquake cycle: Constraints from the time-dependent depth distribution of aftershocks, *Geophys. Res. Lett.* **31,** L23610 , doi: 10.1029/2004GL021379.

Schlupp, A., and A. Cisternas (2007). Source history of the 1905 great Mongolian earthquakes (Tsetserleg, Bolnay), *Geophys. J. Int.* **169,** 1115–1131.

Scholz, C. H., C. A. Aviles, and S. G. Wesnousky (1986). Scaling differences between large intraplate and interplate earthquakes, *Bull. Seismol. Soc. Am.* **76,** 65–70.

Shaw, B. E. (2009). Constant stress drop from small to great earthquakes in magnitude-area scaling, *Bull. Seismol. Soc. Am.* **99,** no. 2A, 871–875.

Shaw, B. E., and S. G. Wesnousky (2008). Slip-length scaling in large earthquakes: The role of deep-penetrating slip below the seismogenic layer, *Bull. Seismol. Soc. Am.* **98,** 1633–1641.

Somerville, P., K. Irikura, R. Graves, S. Sawada, D. Wald, N. Abrahamson, Y. Iwasaki, T. Kagawa, N. Smith, and A. Kowada (1999). Characterizing crustal earthquake slip models for the prediction of strong ground motion, *Seismol Res. Lett.* **70,** 199–222.

Stirling, M. W., and J. G. Anderson (2018). Magnitude as a function of rupture length and slip rate for recent large New Zealand earthquakes, *Bull. Seismol. Soc. Am.* **108,** no. 3B, 1623–1629, doi: 10.1785/0120170284.

Stirling, M. W., G. H. McVerry, and K. R. Berryman (2002). A new seismic hazard model for New Zealand, *Bull. Seismol. Soc. Am.* **92,** no. 5, 1878–1903.

Tocher, D. (1958). Earthquake energy and ground breakage, *Bull. Seismol. Soc. Am.* **48,** 147–153.

Wells, D. L., and K. J. Coppersmith (1994). New empirical relationships among magnitude, rupture length, rupture width, rupture area, and surface displacement, *Bull. Seismol. Soc. Am.* **84,** no. 4, 974–1002.

Yang, W., Z. Peng, B. Wang, Z. Li, and S. Yuan (2015). Velocity contrast along the rupture zone of the 2010 Mw6.9 Yushu, China, earthquake from fault zone head waves, *Earth Planet. Sci. Lett.* **416,** 91–97.

Manuscript received 16 April 2021
Published online 7 September 2021